INSTITUTE OF PHYSICS PUBLISHING JOURNAL OF PHYSICS B: ATOMIC, MOLECULAR AND OPTICAL PHYSICS

J. Phys. B: At. Mol. Opt. Phys. **36** (2003) 1645–1662 PII: S0953-4075(03)59190-8

Quantum mechanical scattering calculations for charge exchange: $O + H^+ \leftrightarrow O^+ + H$

J A Spirko[1], J J Zirbel[2] and A P Hickman[3,4]

[1] Department of Chemistry, Lehigh University, Bethlehem, PA 18015, USA
[2] Department of Physics and JILA, University of Colorado, Boulder, CO 80309-0440, USA
[3] Department of Physics, Lehigh University, Bethlehem, PA 18015, USA

E-mail: spirko@yahoo.com and aph2@lehigh.edu

Received 3 February 2003, in final form 3 March 2003
Published 3 April 2003
Online at stacks.iop.org/JPhysB/36/1645

Abstract

Thermal energy collisions of oxygen atoms with protons ($O + H^+$) may lead to fine-structure excitation of the oxygen or to charge exchange ($O^+ + H$). The reverse process, collisions of oxygen ions with hydrogen, may also lead to charge exchange. Detailed quantum mechanical calculations of these processes are presented here. The potential curves and coupling terms of $^3\Sigma^-$ symmetry used are those recently calculated by Spirko *et al* (2000 *J. Phys. B: At. Mol. Opt. Phys.* **33** 2395–407). The other necessary potentials, the A $^3\Pi$ and $^5\Sigma$ curves, were taken from the literature. Cross sections for charge exchange and fine-structure excitation are reported. For several transitions, mechanisms based on curve crossings are proposed. The analysis indicates that the scattering cross sections are sensitive to the form of the molecular potentials for internuclear distances of 10–15 a_0. The only point of comparison with experiment is for rate constants for charge exchange, averaged over fine-structure levels. The present results, as well as other recent calculations, lie within the large error bars of the limited experimental data.

1. Introduction

The ionization potentials of $O(^3P_1)$ and H atoms differ by less than 0.01 cm^{-1}. This near-degeneracy means that the charge exchange processes

$$O + H^+ \leftrightarrow O^+ + H$$

have very large cross sections in both directions. These processes play central roles in interactions with the solar wind, in atomic escape in the exospheres of Venus, Earth, and Mars, and also in interstellar clouds. Detailed cross sections are needed for modelling. However,

[4] Author to whom any correspondence should be addressed.

only a few experimental studies are available [1, 2], and two recent theoretical studies [3, 4] are not in complete agreement.

We recently performed *ab initio* electronic structure calculations of potentials and coupling terms for several $^3\Sigma^-$ states of OH^+ [5]. We now report quantum mechanical coupled channels calculations based on these potentials. Spin-orbit coupling is included, and we present cross sections for charge exchange and fine-structure excitation as a function of collision energy. We have also calculated rate constants for comparison with the limited amount of experimental data.

The calculations described in our previous work [5] provide most of the information needed for the present calculations. Section 2 describes the remaining analysis needed to formulate and solve the scattering problem. Section 3 discusses our results. We find that many of the calculated results may be understood using well-known models. For several transitions, collision mechanisms based on curve crossings have been identified. We also identify the crucial role played by long-range coupling terms. Section 4 is a summary.

2. Theory

The issue we address in this section is the selection of an appropriate angular momentum basis set to describe the states of the OH^+ system. The essential problem is that different parts of our calculations are most conveniently formulated using different angular momentum coupling schemes. Each scheme is associated with a set of quantum numbers and corresponds to a particular basis set for a vector space. We must determine the unitary transformations that relate the basis sets and then transform all parts of the computational problem to a common basis.

2.1. Quantum states, channels and basis sets

The channels (or basis functions) used in the scattering calculation are determined by the states of the OH^+ system. However, different sets of states are used at successive stages of our calculations. The electronic structure calculations presented in [5] were, like most such calculations, performed using LS coupling. These calculations neglect spin-orbit coupling, which is very important in the OH^+ molecule because of the near-degeneracy of asymptotic fine-structure energy levels. We can include these effects, but in the analysis we must describe the states of the oxygen atom using an alternative scheme, JJ coupling. Finally, both the LS and JJ coupling schemes are applied to the fixed-nuclei problem. Inclusion of the nuclear motion, which of course is essential for the scattering process, leads to a third set of states that correspond exactly to the channels in the scattering process.

The LS and JJ coupling schemes provide a prescription for constructing the angular momentum states of a composite system from the states of the individual parts. For the OH^+ molecule in the fixed-nuclei case, there are four individual angular momenta. The operators for the electronic orbital and spin angular momentum of the oxygen atom or ion are denoted by $\boldsymbol{L}_1$ and $\boldsymbol{S}_1$. The corresponding operators for the hydrogen atom or ion are $\boldsymbol{L}_2$ and $\boldsymbol{S}_2$. Their sum will be denoted by $\boldsymbol{K}$:

$$\boldsymbol{K} = \boldsymbol{L}_1 + \boldsymbol{S}_1 + \boldsymbol{L}_2 + \boldsymbol{S}_2. \tag{1}$$

Because there are several ways to add individual angular momenta together to produce a given $\boldsymbol{K}$, the various alternatives correspond to distinct quantum states. In the following sections we discuss several of these alternatives and show how each is appropriate for a different part of our analysis.

Table 1. Quantum numbers in LS coupling. The states with different $|M_L|$ are separated to show the correspondence with the spectroscopic terms.

	γ								
Charge state	L_1	S_1	L_2	S_2	L	M_L	S	M_S	Term
$O + H^+$	1	1	0	0	1	0	1	$0, \pm1$	$X\,^3\Sigma^-$
					1	±1	1	$0, \pm1$	$A\,^3\Pi$
$O^+ + H$	0	3/2	0	1/2	0	0	1	$0, \pm1$	$2\,^3\Sigma^-$
					0	0	2	$0, \pm1, \pm2$	$1\,^5\Sigma^-$

Table 2. Quantum numbers in JJ coupling. Asymptotic energy levels are given.

Charge state	J_1	J_2	K	M_K	Energy (cm^{-1})
$O(^3P_2) + H^+$	2	0	2	$0, \pm1, \pm2$	0.0
$O(^3P_1) + H^+$	1	0	1	$0, \pm1$	158.265
$O(^3P_0) + H^+$	0	0	0	0	226.977
$O^+ + H$	3/2	1/2	1	$0, \pm1$	158.256
$O^+ + H$	3/2	1/2	2	$0, \pm1, \pm2$	

2.2. LS coupling

Molecular potential curves are usually calculated in the LS coupling scheme. The angular momenta are added together as follows:

$$\boldsymbol{L} = \boldsymbol{L}_1 + \boldsymbol{L}_2, \qquad \boldsymbol{S} = \boldsymbol{S}_1 + \boldsymbol{S}_2.$$

The quantum numbers in this basis are L_1, S_1, L_2, S_2, L, M_L, S and M_S. Letting γ stand for $\{L_1, S_1, L_2, S_2\}$, we can represent the basis states by $|\gamma L M_L S M_S\rangle$. Then γ effectively denotes the charge state. The possible values of the quantum numbers in LS coupling are shown in table 1. The diabatic potential curves and coupling terms for $^3\Sigma^-$ symmetry calculated by Spirko *et al* [5] correspond to selected matrix elements of the electronic Hamiltonian $H_{\rm elec}$ in the LS basis set. The general expression that includes LS potential curves of other symmetries is

$$\langle \gamma' L' M'_L S' M'_S | H_{\rm elec} | \gamma L M_L S M_S \rangle = \delta_{\gamma'\gamma}\delta_{L'L}\delta_{M'_L M_L}\delta_{S'S}\delta_{M'_S M_S} V_{L M_L S M_S}(R) + (1 - \delta_{\gamma'\gamma})\delta_{S1}\delta_{\Lambda 0} Q(R). \tag{2}$$

The first term on the right gives the diagonal diabatic potentials for the sets of quantum numbers listed in table 1. For the two $^3\Sigma^-$ states, we use the curves denoted $H_{11}(R)$ and $H_{22}(R)$ by Spirko *et al* [5]. These two diabatic states correspond to the two possible charge states, and they are coupled by the $Q(R)$ term, which was denoted $H_{12}(R)$ by Spirko *et al*. For the $A\,^3\Pi$ and $1\,^5\Sigma$ potentials, we use the previous calculations of Saxon and Liu [6] and Chambaud *et al* [3], respectively.

Conventional notation is to use $\Lambda = |M_L|$ and $\Omega = M_L + M_S$ instead of M_L and M_S. Ω is the z component of the total electronic angular momentum, and $H_{\rm elec}$ is block diagonal in Ω. When spin-orbit effects (denoted by $H_{\rm so}$) are included, $H_{\rm elec} + H_{\rm so}$ will also be block diagonal in Ω.

2.3. JJ coupling

In this paper, we are concerned with transitions between states of the OH^+ molecule in the separated atom limit. A crucial feature in this limit is the existence of distinct fine-structure

levels of oxygen, $O(^3P_J)$, $J = 2, 1, 0$. The energies of these levels are given in table 2. In order to include these levels properly in our calculation, we extend our theoretical model using the methodology developed by Cohen and Schneider [7] and Hickman *et al* [8].

The fine-structure effects can be modelled by adding an additional operator to the Hamiltonian:

$$H_{\mathrm{so}} = \xi \boldsymbol{L}_1 \cdot \boldsymbol{S}_1. \tag{3}$$

This operator only involves the oxygen atom. An explicit value of ξ is not needed, since we will use the experimental energies directly as shown below. The matrix elements of H_{so} are most conveniently expressed if one adopts the *JJ* angular momentum coupling scheme:

$$\boldsymbol{J}_1 = \boldsymbol{L}_1 + \boldsymbol{S}_1, \qquad \boldsymbol{J}_2 = \boldsymbol{L}_2 + \boldsymbol{S}_2, \qquad \boldsymbol{K} = \boldsymbol{J}_1 + \boldsymbol{J}_2.$$

The angular momentum quantum numbers in this scheme are L_1, S_1, L_2, S_2 (again denoted collectively by γ), J_1, J_2, K, and M_K, and the basis states can be written $|\gamma J_1 J_2 K M_K\rangle$. Since the total angular momentum $\boldsymbol{J}_1$ of the oxygen atom is explicitly constructed, this basis is appropriate for describing the fine-structure levels of oxygen. The matrix representation of H_{so} in *JJ* coupling is diagonal, and we can set the diagonal matrix elements to the experimental values:

$$\langle \gamma' J_1' J_2' K' M_K' | H_{\mathrm{so}} | \gamma J_1 J_2 K M_K \rangle = \delta_{\gamma'\gamma} \delta_{J_1' J_1} \delta_{J_2' J_2} \delta_{K',K} \delta_{M_K', M_K} E_{J_1}. \tag{4}$$

In this basis M_K is equivalent to Ω, and the above expression shows explicitly that H_{so} does not couple states with different Ω. The matrix element is set to zero for charge states corresponding to $O^+ + H$.

2.4. Full fixed-nuclei Hamiltonian

In the two previous sections we determined explicit formulae for the matrix representations of H_{elec} and H_{so}. The full fixed-nuclei Hamiltonian for the OH^+ molecule is just the sum of these two operators. However, equations (2) and (4) are expressed in different basis sets so we must transform H_{elec} to the *JJ* basis set. The transformation needed can be determined by evaluating the matrix elements between the states of the *LS* and *JJ* basis sets:

$$\begin{aligned}\langle \gamma LS\Lambda\Omega | \gamma J_1 J_2 K \Omega \rangle = (-1)^{S-L-\Omega} \sqrt{(2K+1)(2L+1)(2S+1)(2J_1+1)(2J_2+1)} \\ \times \begin{pmatrix} L & S & K \\ \Lambda & \Omega-\Lambda & -\Omega \end{pmatrix} \begin{Bmatrix} L_1 & L_2 & L \\ S_1 & S_2 & S \\ J_1 & J_2 & K \end{Bmatrix}.\end{aligned} \tag{5}$$

In this expression, $(\cdots)$ and $\{\cdots\}$ represent $3j$ symbols and $9j$ symbols, respectively.

2.5. Final coupled equations and cross section formulae

Up until this point, we have been discussing the 'fixed-nuclei' Hamiltonian. The states of this Hamiltonian are calculated under the assumption that the nuclei are not moving. Much of the effort to determine these matrix elements required large-scale numerical calculations specifically undertaken for the OH^+ molecule. The next stage of the calculation, in which the nuclear motion is introduced, follows closely work already available in the literature [8–11]. Here we only summarize the main ideas and final formulae used.

When nuclear motion is included, the orbital angular momentum $\boldsymbol{\ell}$ must be added to the $\boldsymbol{K}$ defined for the fixed-nuclei system to give the grand total

$$\boldsymbol{P} = \boldsymbol{K} + \boldsymbol{\ell}. \tag{6}$$

Table 3. List of channels in the basis set used for calculations. The two sets have opposite parities and do not mix. Channels with $\Omega = 0$ appear with one parity or the other, while those with $\Omega \geqslant 1$ appear with both parities. Only those channels with $\Omega \leqslant P$ are allowed, so for $P = 0$, for example, the two sets have only 3 and 2 channels, respectively.

9-channel set, even parity					8-channel set, odd parity				
i	J_1	J_2	K	Ω	i	J_1	J_2	K	Ω
1	2	0	2	0	1	2	0	2	1
2	2	0	2	1	2	2	0	2	2
3	2	0	2	2	3	3/2	1/2	1	1
4	3/2	1/2	1	0	4	3/2	1/2	2	0
5	3/2	1/2	1	1	5	3/2	1/2	2	1
6	3/2	1/2	2	1	6	3/2	1/2	2	2
7	3/2	1/2	2	2	7	1	0	1	0
8	1	0	1	1	8	1	0	1	1
9	0	0	0	0					

Table 4. Matrix elements of $H_{\rm elec}$ between the channels in the JJ basis. $H_{\rm elec}$ is block diagonal with respect to Ω and parity; each block is shown separately. The $1\,^5\Sigma^-$ states, for which $J_1 = 3/2$ and $K = 2$, are omitted because they are always uncoupled from the other states. The rows and columns of each block are associated with the channel index i given in table 3. For each 3×3 (1×1) block there are three (one) channels of the appropriate parity and Ω. V_X and V_2 are the diagonal diabatic potentials for the $X\,^3\Sigma^-$ and $2\,^3\Sigma^-$ states, respectively, and Q is the off-diagonal element for this block. V_Π is the potential for the $A\,^3\Pi$ state.

$\Omega = 0$ Even parity			$\Omega = 0$ Odd parity
$\frac{1}{3}(2V_X + V_\Pi)$	$\sqrt{\frac{2}{3}}Q$	$\frac{\sqrt{2}}{3}(V_\Pi - V_X)$	V_Π
$\sqrt{\frac{2}{3}}Q$	V_2	$-\sqrt{\frac{1}{3}}Q$	
$\frac{\sqrt{2}}{3}(V_\Pi - V_X)$	$-\sqrt{\frac{1}{3}}Q$	$\frac{1}{3}(V_X + 2V_\Pi)$	
$\Omega = 1$ Both parities			$\Omega = 2$ Both parities
$\frac{1}{2}(V_X + V_\Pi)$	$\sqrt{\frac{1}{2}}Q$	$\frac{1}{2}(V_\Pi - V_X)$	V_Π
$\sqrt{\frac{1}{2}}Q$	V_2	$-\sqrt{\frac{1}{2}}Q$	
$\frac{1}{2}(V_\Pi - V_X)$	$-\sqrt{\frac{1}{2}}Q$	$\frac{1}{2}(V_X + V_\Pi)$	

New states $|\gamma J_1 J_2 K \ell P M_P\rangle$ can be defined that include the extra degrees of freedom. These states will be used to express the final T matrix elements. However, we formulate the numerical solution of the coupled equations by starting with a body-fixed basis [8–11], which we denote by $|\gamma J_1 J_2 K M_K P M_P\rangle$. We then construct linear combinations of the pair of states $|\gamma J_1 J_2 K M_K P M_P\rangle$ and $|\gamma J_1 J_2 K (-M_K) P M_P\rangle$ to form eigenstates of parity (eigenvalue $\epsilon = \pm 1$). Using the notation $\Omega = M_K$ and taking $\Omega > 0$, we have

$$|\gamma J_1 J_2 K \Omega \epsilon P M_P\rangle = \frac{1}{\sqrt{2}}[|\gamma J_1 J_2 K M_K P M_P\rangle + \epsilon\epsilon_1\epsilon_2|\gamma J_1 J_2 K (-M_K) P M_P\rangle]. \tag{7}$$

ϵ_1 and ϵ_2 are the parities of the oxygen and hydrogen atoms, respectively. The parities of the atoms are $\epsilon_{O^+} = -1$ and $\epsilon_O = \epsilon_H = \epsilon_{H^+} = 1$. Channels with $\Omega = 0$ are already either odd or even parity. The channels in the body-fixed JJ coupled basis with parity are listed in table 3.

For each value of P, the 17 channels split into a set of eight of one parity and a set of nine of the other. Matrix elements for $H_{\rm elec}$ in the states $|\gamma J_1 J_2 K \Omega \epsilon P M_P\rangle$ are given in table 4.

In the body-fixed formulation the final scattering equations may be written as

$$\sum_k \left[\frac{\mathrm{d}^2}{\mathrm{d}R^2}\delta_{jk} - 2\mu(V_{\rm rot}^{jk} + H_{\rm elec}^{jk} + H_{\rm so}^{jk}) + k_i^2\delta_{jk} \right] F_{i\to k}^{P\epsilon} = 0 \tag{8}$$

where the indices i, j, and k represent states in the $|\gamma J_1 J_2 K \Omega \epsilon P M_P\rangle$ basis. The advantage of the body-fixed basis is that the matrix elements of $H_{\rm elec}$ and $H_{\rm so}$ may be directly adapted from our previous development of the fixed-nuclei Hamiltonian. Additional terms denoted by $V_{\rm rot}$ arise because of the nuclear motion. Briefly, $V_{\rm rot}$ is the centrifugal potential

$$V_{\rm rot} = \frac{\ell^2}{2\mu R^2}. \tag{9}$$

It is diagonal in the $|\gamma J_1 J_2 K \ell P M_P\rangle$, but when it is transformed to the $|\gamma J_1 J_2 K \Omega \epsilon P M_P\rangle$ basis, there are also off-diagonal terms connecting channels with a given Ω with channels with $\Omega \pm 1$. Explicit expressions for the matrix elements of $V_{\rm rot}$ are given by Launay [11].

The solutions to equation (8) are determined using our standard code, which implements the log-derivative method [12]. In the asymptotic region, the numerical solutions are transformed to the space-fixed $|\gamma J_1 J_2 K \ell P M_P\rangle$ basis and then used to determine the T matrix elements. The final expressions for the cross sections may be written in the usual way:

$$\sigma_{J_1 J_2 \to J_1' J_2'} = \frac{\pi}{k_{J_1 J_2}^2 (2J_1+1)(2J_2+1)} \times \sum_{P=0}^{\infty}(2P+1) \sum_{K=|J_1-J_2|}^{J_1+J_2} \sum_{K'=|J_1'-J_2'|}^{J_1'+J_2'} \sum_{\ell=|P-K|}^{P+K} \sum_{\ell'=|P-K'|}^{P+K'} |T^P_{J_1' J_2' K' \ell', J_1 J_2 K \ell}|^2. \tag{10}$$

3. Results and discussion

The formalism described in the last section has been implemented, and cross sections for collisions of O^+ and H (and O and H^+) have been calculated over a wide energy range. Figure 1 provides an overview of the results. Cross sections are shown for all of the upward transitions for total energies ranging from threshold values to 7000 cm^{-1}. Since each of the asymptotic energy levels of OH^+ that we consider has a unique value of J_1, the angular momentum quantum number of the oxygen species, we use this quantum number as a label for the various cross sections. Thus, the transition labelled $2 \to 3/2$ refers to the initial state $O(^3P_2) + H^+$ and to the final state $O^+(^4S_{3/2}) + H$. Here we note several general features of our results.

The charge exchange cross section $3/2 \to 1$ has a sharp peak just above threshold, and then falls off rapidly. In fact, our calculated cross sections exhibit a peak that reaches several thousand a_0^2 and has a width of about 0.03 cm^{-1}. This feature arises because of the near-degeneracy of the $J_1 = 3/2$ and 1 asymptotic levels; the detailed structure of the peak is uncertain because of the difficulty in determining the coupling terms at very large internuclear separations. The broad features of the cross section for $3/2 \to 1$ shown in the diagram arise from other coupling terms that are more reliably determined. For energies greater than about 500 cm^{-1}, the dominant cross section is for the $2 \to 1$ transition. For total energies greater than about 1500 cm^{-1}, the next largest cross section is for the $2 \to 3/2$ transition.

The calculations were performed at energies spaced sufficiently close together to enable us to determine rate constants for temperatures in the range from 10 to 1000 K. The spacing ranged from 0.1 cm^{-1} near threshold, to 50 cm^{-1} for total energies $E > 1000$ cm^{-1}. In addition, since calculations like the present one may be expected to exhibit numerous 'orbiting

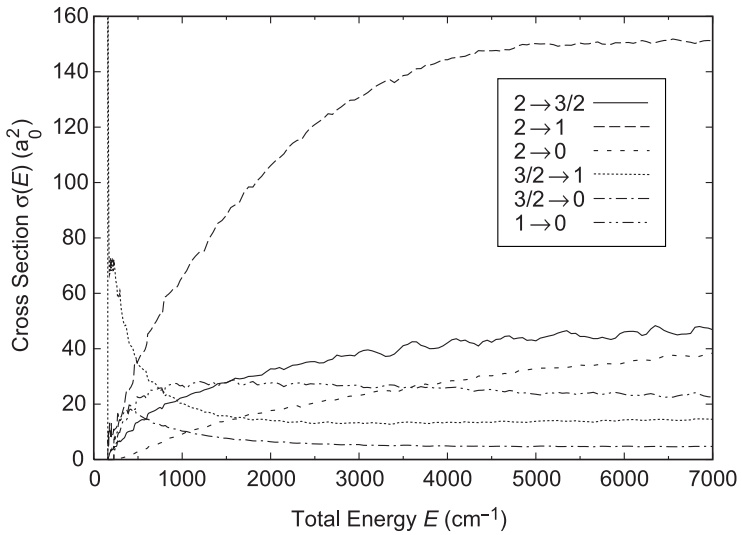

Figure 1. Calculated cross sections for all upward transitions as a function of total energy. The total energy includes the internal energy of the atoms in their initial states relative to $O(^3P_2) + H^+$. As described in the text, the states are labelled by the value of the quantum number J_1 of the oxygen species ($J_1 = 0$, 1, and 2 for O and 3/2 for O^+).

resonances', we performed a detailed search for narrow structure in selected energy ranges. Indeed, many extremely narrow features (widths of order 0.1 cm^{-1}) were identified. These features are too narrow to be seen in figure 1, and they do not affect the rate constants.

Our calculations have produced a large amount of numerical data. These results reflect coupling among a large number of channels, and it is often difficult to associate certain transitions with specific coupling terms, particularly for the smaller cross sections. However, we were able to construct reasonable hypotheses about the likely mechanisms that lead to some of the larger cross sections.

Finally, we will usually discuss only upward transitions. Because the T matrix is symmetric, any transition from a level i to a level j is related to the reverse transition $j \rightarrow i$ by the principle of detailed balance.

3.1. Scattering mechanisms

Here we investigate possible mechanisms that could contribute to the inelastic cross sections. We base our discussion on well-known models involving classical trajectories and localized curve crossings. Figure 2 gives the radial adiabatic potentials, which were obtained by diagonalizing $H_{elec} + H_{so}$ at each value of R. One can use these curves to visualize the collision. The particles begin far apart and then approach, following a trajectory determined by the appropriate adiabatic potential curve. The particles are assumed to follow a single curve until an interaction causes them to cross from one curve to another. In the idealized picture, these interactions occur only near crossing points at certain critical values of R. During the trajectory, the particles may undergo one or more such curve crossings. The state at the end of the collision is determined by the final curve the particles follow as they separate. This picture is the basis of many collision studies, and in the present case we find it gives considerable physical insight into the mechanisms of the collision process.

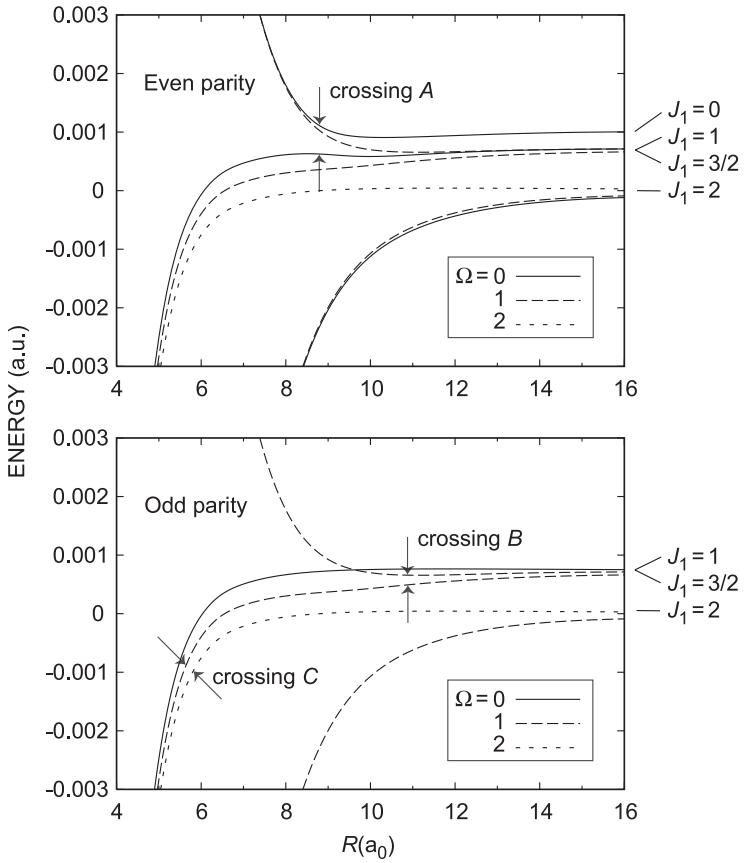

Figure 2. Radial adiabatic potential curves obtained by diagonalizing $H_{\rm elec} + H_{\rm so}$. There are 17 channels, which split into nine of even parity and eight of odd parity. Five curves arising from the $1\,^5\Sigma^-$ state are completely uncoupled from the other states and are not shown. The potential curve crossings *A*, *B* and *C* discussed in the text are shown. Crossing *A* involves an $\Omega = 0$ state that exists only in even parity. Crossings *B* and *C* may occur in either parity.

3.2. Identification of curve crossings

Several situations can lead to radial or rotational coupling among the adiabatic radial potentials shown in figure 2. In the adiabatic picture, radial coupling appears as a strong R-dependence of the coefficients of the adiabatic eigenvectors obtained by diagonalizing the matrices representing $H_{\rm elec} + H_{\rm so}$. Rotational coupling terms are defined by Launay [11] and explicitly couple two adiabatic potential curves whose values of Ω satisfy $|\Delta\Omega| = 1$.

For both radial and rotational coupling, one identifies a critical value $R = R_{\rm c}$ at which a transition from one curve to another may occur. Two standard models [13] are the Landau–Zener model and the Demkov model. In the Landau–Zener model, two diabatic potentials (say $H_{ii}(R)$ and $H_{jj}(R)$) cross at $R_{\rm c}$, and the off-diagonal term $H_{ij}(R)$ gives an amplitude for a transition at that crossing point. In the Demkov model the diabatic curves H_{ii} and H_{jj} are assumed to be parallel, and the off-diagonal term H_{ij} increases exponentially. The point $R_{\rm c}$ is the value of R for which the coupling term $H_{ij}(R)$ is equal to half the difference $H_{ii}(R) - H_{jj}(R)$. For both of these models an important parameter is the so-called 'Massey

parameter' α, given by [14]

$$\alpha = \frac{a\Delta E}{\hbar v}, \tag{11}$$

where ΔE is the energy difference between the adiabatic potentials, v is the radial velocity at the crossing point, and a is the distance over which the main effect of the coupling takes place. If H_{ij} has a typical exponential form $A\mathrm{e}^{-r/r_0}$, then r_0 is this distance. The Massey parameter is the ratio of the time it takes for the particles to traverse the interaction region (a/v) to the Heisenberg uncertainty time $\Delta t = \hbar/\Delta E$. The case $\alpha \ll 1$ corresponds to the 'sudden limit' (curve crossings are likely), and $\alpha \gg 1$ corresponds to the 'adiabatic limit' (the particles tend to follow the adiabatic curves).

We have identified several regions of the adiabatic potential curves shown in figure 2 where curve crossings might take place. In each of these regions one of the idealized models may be invoked. For example, for the even-parity states shown in figure 2 there is an avoided crossing of the two highest $\Omega = 0$ curves. We have labelled this feature 'crossing A'. The Landau–Zener model is appropriate, and the corresponding diabatic potentials cross near $R_c = 8.6\,a_0$. In the region $7\,a_0 < R < 10\,a_0$, the $\mathrm{d}/\mathrm{d}R$ matrix elements between the eigenvectors attain large values due to this crossing. Crossing A occurs only for even parity. In another example, marked 'crossing B' in figure 2, the diabatic radial potentials with $\Omega = 1$ that asymptotically approach the $J_1 = 1$ and $3/2$ levels exhibit behaviour similar to a Demkov crossing. The arrows indicate the critical distance R_c, where the coupling is half the difference between the curves. The third example illustrates that rotational coupling can also provide the off-diagonal matrix element at a crossing. For internuclear distances of about 4–6 a_0, the three A $^3\Pi$ states in both symmetries interact via rotational coupling. This coupling region is important for transitions from the $J_1 = 2$ level to the $J_1 = 1$ level, as we will discuss below. The most important coupling appears to be between the $\Omega = 1$ and $\Omega = 2$ states. The situation can be described using the Demkov model for the point labelled 'crossing C' in figure 2. Crossings B and C occur both for even and odd parity.

3.3. Supplementary calculations

To investigate further the curve crossing mechanisms discussed here, we performed a few calculations in which some of the coupling terms were modified or even eliminated. In several cases we found that eliminating specific coupling terms led to substantial changes in particular cross sections. Results of this type lend credence to the argument that we can identify specific mechanisms that contribute to certain transitions.

One calculation tested the importance of the rotational coupling terms. These terms are the off-diagonal matrix elements of ℓ^2. Specifically, we set

$$\langle \gamma J_1 J_2 K \Omega \epsilon P M_P | \ell^2 | \gamma J_1 J_2 K (\Omega \pm 1) \epsilon P M_P \rangle = 0. \tag{12}$$

This modification is equivalent to the centrifugal decoupling that Launay [11] labels CD2.

Figure 3 shows the results of removing the rotational coupling. All of the cross sections for fine-structure transitions decrease. The $J_1 = 0$ states are strictly decoupled from the $J_1 = 1$ states in this case. Also, all cross sections involving $J_1 = 2$ states are reduced. The $3/2 \rightarrow 1$ cross section is not significantly affected. An interesting note is that the $3/2 \rightarrow 0$ cross section is actually enhanced when the rotational coupling is removed. Systems starting in the $J_1 = 3/2$ states prefer to end up in the $J_1 = 2$ state, but with $J_1 = 2$ interactions reduced by the elimination of rotational coupling, more systems end up in the $J_1 = 0$ state.

A second calculation was performed with the electronic diabatic coupling $Q(R)$ set to zero. This modification had the effect of decoupling the $O^+ + H$ states from the $O + H^+$ states,

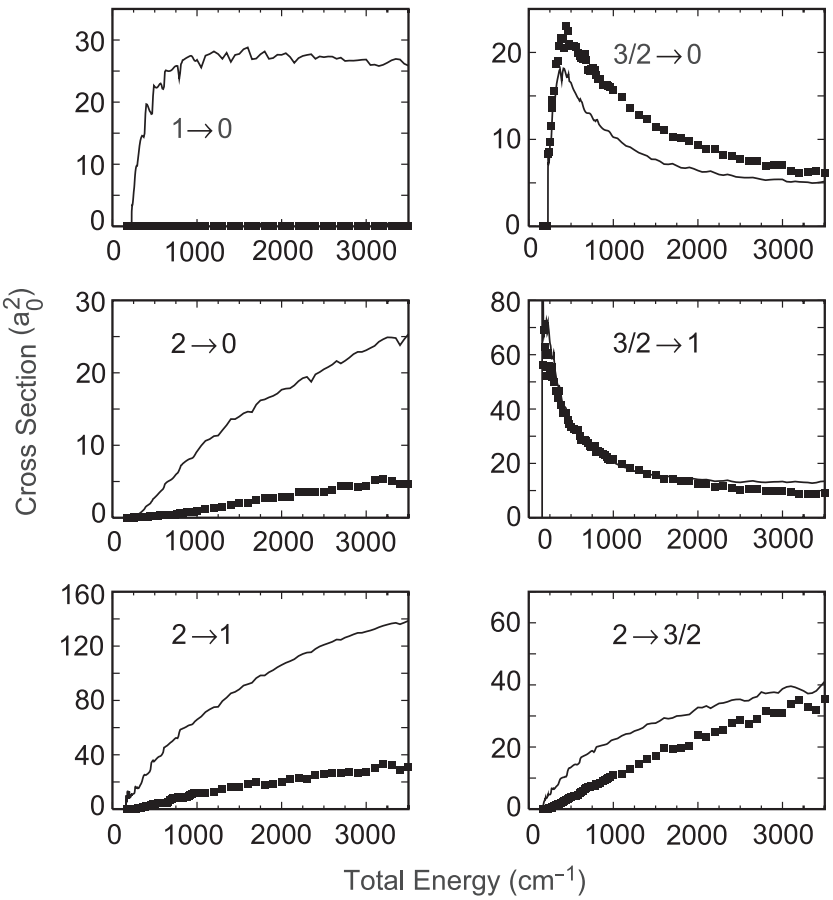

Figure 3. Demonstration of the effect of rotational coupling. Calculations with this coupling fully included (——) are compared with calculations in which the off-diagonal rotational coupling terms are set to zero (■).

so that charge exchange is no longer possible. The effect on fine-structure transitions is small, however. Figure 4 demonstrates that the fine-structure excitation of oxygen by a proton is not greatly affected by the charge exchange channels.

Several calculations were performed with a form of $Q(R)$ modified to have a steeper slope at the crossing point near 11 a_0. The modified $Q(R)$ is shown in figure 5. These calculations were specifically designed to probe the $2 \rightarrow 3/2$ transition, and they will be discussed below.

3.4. The $2 \rightarrow 1$ *transition*

We first examine the $2 \rightarrow 1$ transition, because it has the largest cross section for most energies. Our supplementary calculations indicated that this transition is strongly but not completely dependent upon rotational coupling. These results are shown in figure 3. We suggest that the rotational coupling occurs in the region near crossing C identified in figure 2. The transition begins with the collision partners on the $J_1 = 2$, $\Omega = 2$ curve. The particles follow this curve inward, undergo a crossing to the $J_1 = 1$, $\Omega = 1$ curve near $R = 5.5\ a_0$, and then follow the latter curve for the rest of the trajectory. This mechanism is available for both odd and even parities.

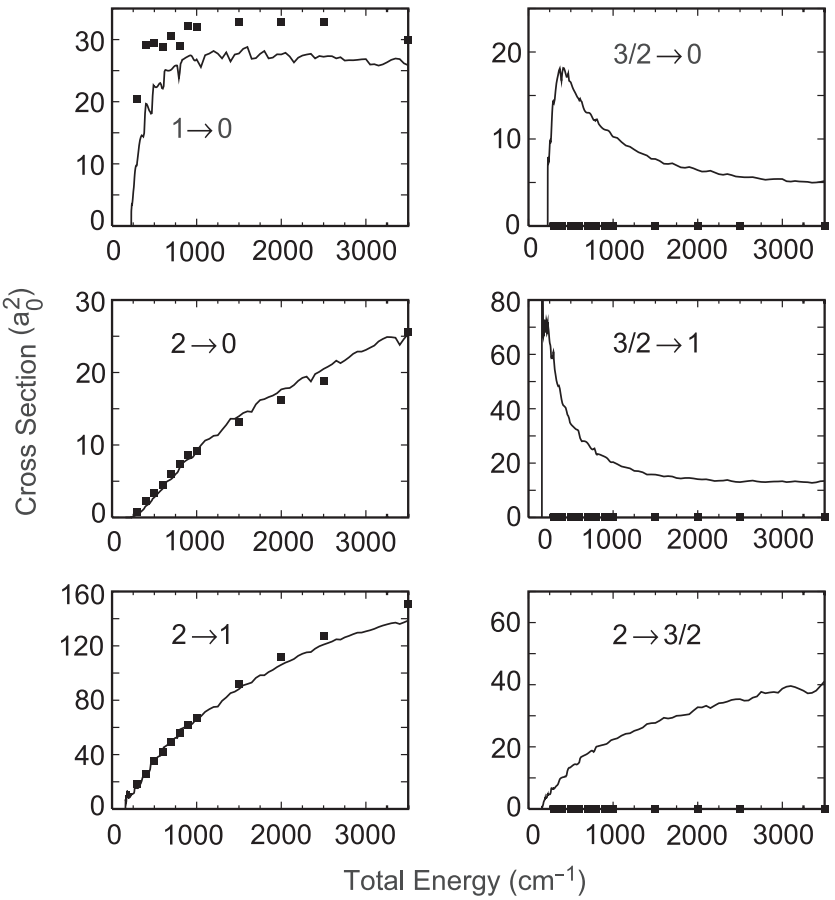

Figure 4. Demonstration of the effect of charge exchange coupling $Q(R)$. Calculations with this coupling fully included (——) are compared with calculations in which $Q(R)$ is set to zero (■).

Figure 3 shows that there is a small cross section for the $2 \rightarrow 1$ transition even when the rotational coupling is eliminated. A mechanism that may account for this residual cross section may be illustrated using figure 2. The transition begins with the particles on a curve with $\Omega = 1$ that correlates with the $J_1 = 2$ level. Near $R = 10\,a_0$, radial coupling at crossing B may cause a transition to another $\Omega = 1$ curve that correlates with the $J_1 = 1$ level. The mechanism is possible for either parity, and it does not involve the charge exchange term $Q(R)$. The latter fact is consistent with the results of the supplementary calculations in which $Q(R)$ was set to zero. As shown in figure 4, the cross section was essentially unchanged in that case.

3.5. The $3/2 \rightarrow 1$ *transition*

The $3/2 \rightarrow 1$ transition is unique because it has little dependence on rotational coupling, as shown in figure 3. Radial coupling at crossing B provides a direct link between these two states. The $J_1 = 1, \Omega = 1$ and $J_1 = 3/2, \Omega = 1$ channels for both parities interact around $R = 11\,a_0$. Figure 5 shows details of the diabatic potentials involved in this crossing. These two potentials are roughly parallel, while the coupling between them is increasing exponentially, making

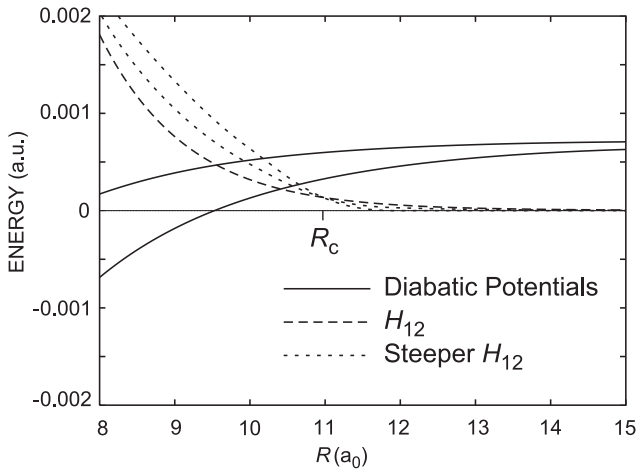

Figure 5. Diabatic potentials for the $J_1 = 1$ and $3/2$ channels with $\Omega = 1$ and the coupling between them. These curves are some of the matrix elements of the diabatic Hamiltonian that was diagonalized to determine the adiabatic potentials shown in figure 2. Shown are the original H_{12} (- - - -) that we calculated and the modified coupling terms (steeper H_{12}, $\cdots\cdots$) that lead to smaller values of the Massey parameter.

this a Demkov crossing. We will discuss the mechanism shown in figure 5 in more detail in section 3.6.

At low energies, the $3/2 \rightarrow 1$ cross section decreases slightly when the rotational coupling is removed. Examination of the separate cross sections for odd and even parity shows that this decrease exists only in the even-parity case. Rotational coupling between the $J_1 = 1$, $\Omega = 1$ and 0 channels allows the latter to participate in transitions to the $J_1 = 3/2$ level, accounting for the lower cross section.

3.6. The $2 \rightarrow 3/2$ *transition*

One likely mechanism that could contribute to the $2 \rightarrow 3/2$ transition is similar to the rotational coupling mechanism proposed for the $2 \rightarrow 1$ transition. The trajectory begins on the $J_1 = 2$, $\Omega = 2$ curve, and a crossing to the $J_1 = 1$, $\Omega = 1$ curve occurs at crossing C near $R = 5.5\ a_0$. If the collision partners separated without further crossing, they would end up in a $J_1 = 1$ state. However, a second crossing is possible as the separating atoms pass through crossing B near 11 a_0 where the $J_1 = 1$, $\Omega = 1$ state and the $J_1 = 3/2$, $\Omega = 1$ are coupled by radial $(\mathrm{d}/\mathrm{d}R)$ terms. If the second crossing occurs, the trajectory leads to the $3/2$ level.

In the course of comparing our results with previous calculations (described in more detail below in section 3.7), we discovered that the $2 \rightarrow 3/2$ transition was extremely sensitive to the details of the coupling term $Q(R)$ near $R = 11\ a_0$. Figure 6 illustrates the effect on the $2 \rightarrow 3/2$ transition caused by small changes in $Q(R)$. The behaviour of the cross section changes dramatically in the energy range from threshold to several hundred wave numbers of energy. We believe that this behaviour can be understood by analysing the curve crossing probability at crossing B (near $R = 11\ a_0$) mentioned above.

Figure 5 illustrates the critical radius R_c, which is located at the point where the coupling term $H_{12}(R)$ is equal to half the energy difference between the diabatic curves. The probability of undergoing a crossing from one adiabatic curve to another is (roughly speaking) determined by the value of the Massey parameter α at the crossing point. For the original coupling terms

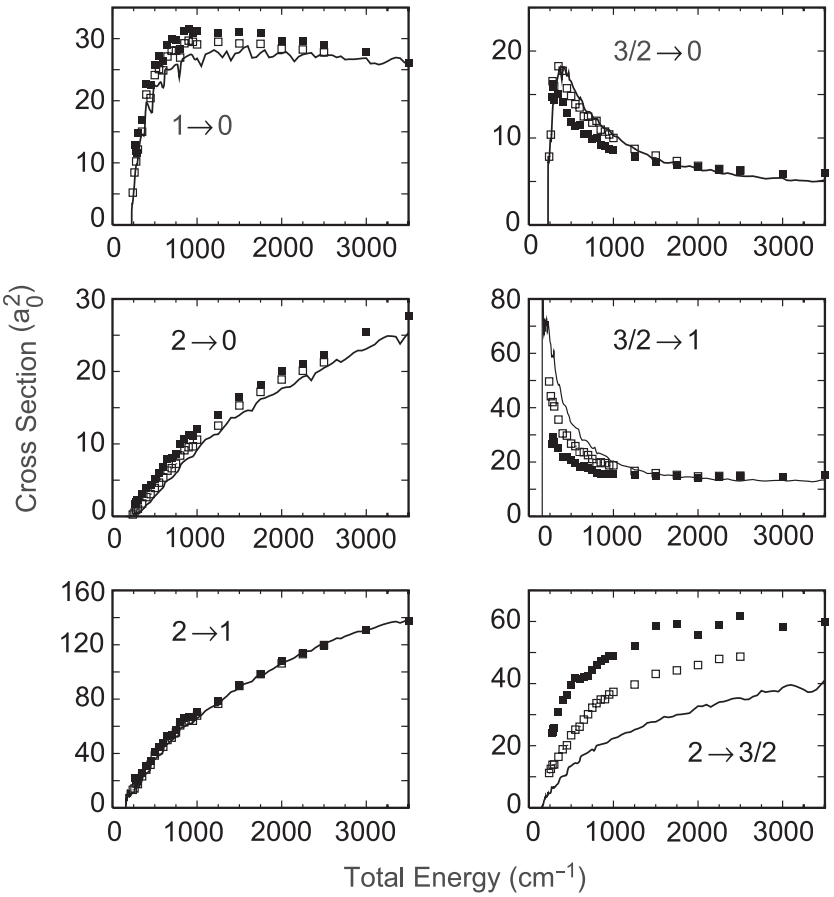

Figure 6. Demonstration of the effect of different values of the Massey parameter α. Calculations were performed using $Q(R)$ as originally calculated (——), for which $\alpha \sim 0.25$ at a total energy of 1000 cm^{-1}. Also shown for comparison are calculations in which $Q(R)$ was modified to make $\alpha \sim 0.12$ (□) and $\alpha \sim 0.08$ (■).

calculated as described in Spirko *et al* [5], the value of α at a total energy of 1000 cm^{-1} is about 0.25. We performed two additional calculations with the coupling $Q(R)$ modified in the range $R \geqslant 7\ a_0$ so that the value of R_c remained the same, but α changed. We could make α smaller by increasing the slope of $Q(R)$. The supplementary calculations shown in figure 5 correspond to $\alpha = 0.12$ and 0.08. The physical picture is that for a steeper $Q(R)$, the coupling region becomes concentrated in a smaller range of distances, and the particle motion is less adiabatic. Hence the curve crossing probability increases. We suggest that this increase accounts for the rapid rise of the $2 \rightarrow 3/2$ cross sections with decreasing values of α as shown in figure 6.

It is interesting to note that the particles traverse crossing B only once during this proposed sequence of crossings. Hence an increased curve crossing probability p leads directly to an increased transition cross section. In the case of the $1 \rightarrow 3/2$ transition discussed earlier, the particles traverse the coupling region twice. A larger value of p can then lead to a smaller cross section, as shown in figure 6.

The mechanism described above depends upon an initial interaction near 5.5 a_0 governed by rotational coupling. Our supplementary calculations show that the cross section for the

$2 \rightarrow 3/2$ transition diminishes when the rotational coupling is set to zero, but there must be another mechanism that does not depend on rotational coupling. Two candidates are the following: for both the $\Omega = 0$ and the $\Omega = 1$ states, off-diagonal matrix elements of $H_{\mathrm{elec}} + H_{\mathrm{so}}$ couple the 2 and $3/2$ channels, as shown in table 4. This coupling provides a path for the transition even when rotational coupling is removed.

3.7. Comparison with previous theoretical results

Figure 7 shows a comparison of the present cross sections with those previously calculated by Chambaud *et al* [3] and by Stancil *et al* [4]. Our results are generally similar to those of Chambaud *et al*. The transitions from one fine-structure level to another in oxygen are particularly close; the biggest differences occur in the charge exchange transitions such as the $2 \rightarrow 3/2$ and the $3/2 \rightarrow 1$. This general similarity is not surprising, because many features of the potentials we used are the same as those of the potentials used by Chambaud *et al*. In 1999, we reported preliminary cross sections [15] that were based on potentials determined by matching those of Chambaud *et al* [3] as closely as possible. Those preliminary results were nearly the same as those of Chambaud *et al* [3]. We used our new $^3\Sigma^-$ curves for the present calculation, but we left the other curves the same. Hence the asymptotic forms for all the diagonal potentials (i.e. $C_3/R^3 + C_4/R^4$) were nearly the same. The major difference is in the new form of $Q(R)$, and we have already noted how sensitive the $2 \rightarrow 3/2$ cross section is to that function. Finally, our supplementary calculations indicated that the fine-structure changing transitions were insensitive to $Q(R)$, so the agreement with Chambaud *et al* [3] for those transitions reflects the use of similar potentials.

Comparison of our results with the calculations of Stancil *et al* [4] (figure 7) reveals several differences. Their $3/2 \rightarrow 1$ and $3/2 \rightarrow 0$ cross sections are qualitatively similar to ours, but their $2 \rightarrow 3/2$ cross sections are much larger and increase to their high-energy limit much more quickly. Stancil *et al* [4] do not present all of the details of their calculation, and so we do not fully understand these differences. We do know [16] that Stancil *et al* [4] used a coupling term $Q(R)$ that was set to zero for $R \geqslant 10.0\ a_0$. Our own investigation suggests that this approximation is not justified. We have emphasized the sensitivity of the $2 \rightarrow 3/2$ transition to the exact form of $Q(R)$ near the coupling region near 11 a_0, and it is for exactly this transition that our results differ most from those of Stancil *et al* [4].

In the next section, we consider to what extent experimental results can distinguish between the various theoretical calculations presented here.

3.8. Comparison with experiment

Experimental data for comparison with the available theoretical calculations are scarce. Two measurements of the rate constant for charge exchange exist; we can compare with these measurements by taking a suitable average of our theoretical results. The rate constant is the thermal average of velocity times the cross section. Transforming to an integral over energy yields

$$\alpha_{J_1 J_2 \rightarrow J_1' J_2'}(T) = \bar{v} \int_0^\infty \sigma_{J_1 J_2 \rightarrow J_1' J_2'}(E_{\mathrm{k}} + E_{J_1 J_2}) \frac{E_{\mathrm{k}} \mathrm{e}^{-E_{\mathrm{k}}/kT}}{(kT)^2}\, \mathrm{d}E_{\mathrm{k}}, \tag{13}$$

where $\bar{v} = \sqrt{8kT/\pi\mu}$ is the mean thermal velocity, E_{k} is the initial kinetic energy of the collision, and $E_{J_1 J_2}$ is the initial internal energy. Note that the calculated cross sections depend on the total energy $E_{\mathrm{k}} + E_{J_1 J_2}$.

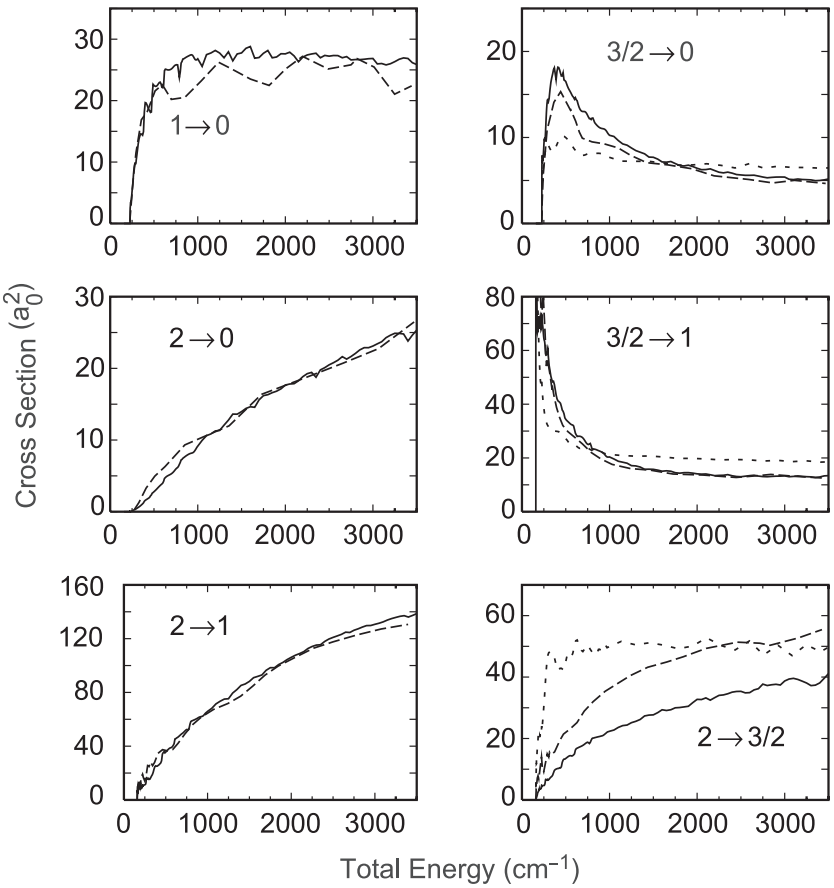

Figure 7. Comparison of the cross sections calculated in this work (——) with other theoretical calculations: Chambaud *et al* (— — —), Stancil *et al* (- - - -).

We now average the state-to-state rates over the populations of each possible initial state and sum over each final state. The final expressions are

$$\alpha_{O^+ + H \to O + H^+}(T) = \sum_{J_1'=2,1,0} \alpha_{\frac{3}{2}\frac{1}{2} \to J_1' 0}(T) \tag{14}$$

$$\alpha_{O + H^+ \to O^+ + H}(T) = \frac{\sum_{J_1=2,1,0}(2J_1+1)\exp(-E_{J_1 0}/kT)\alpha_{J_1 0 \to \frac{3}{2}\frac{1}{2}}(T)}{\sum_{J_1=2,1,0}(2J_1+1)\exp(-E_{J_1 0}/kT)}. \tag{15}$$

Experimental results are available for both directions of the collision at 300 K. Both Chambaud *et al* and Stancil *et al* calculated rate coefficients at several temperatures. Figure 8 shows a comparison of the present results with those just mentioned. All theoretical calculations of the rate coefficients at 300 K are within the large error bars of the experiments.

Chambaud *et al* [3] calculated state-averaged rate coefficients in the $O^+ + H \to O + H^+$ direction, except for $T = 300$ K, where they calculated the rate in the other direction. For the available points, the rates of Chambaud *et al* are always higher than ours, owing to the discrepancy in the $2 \to 3/2$ cross section. We calculated the rates for the calculations of Stancil *et al* [4] using corrected cross sections [16]. All of their state-averaged rate coefficients are greater than ours as well, because for low energies, their $2 \to 3/2$ cross sections are much greater, while for higher energies, their $3/2 \to 1$ cross sections are larger.

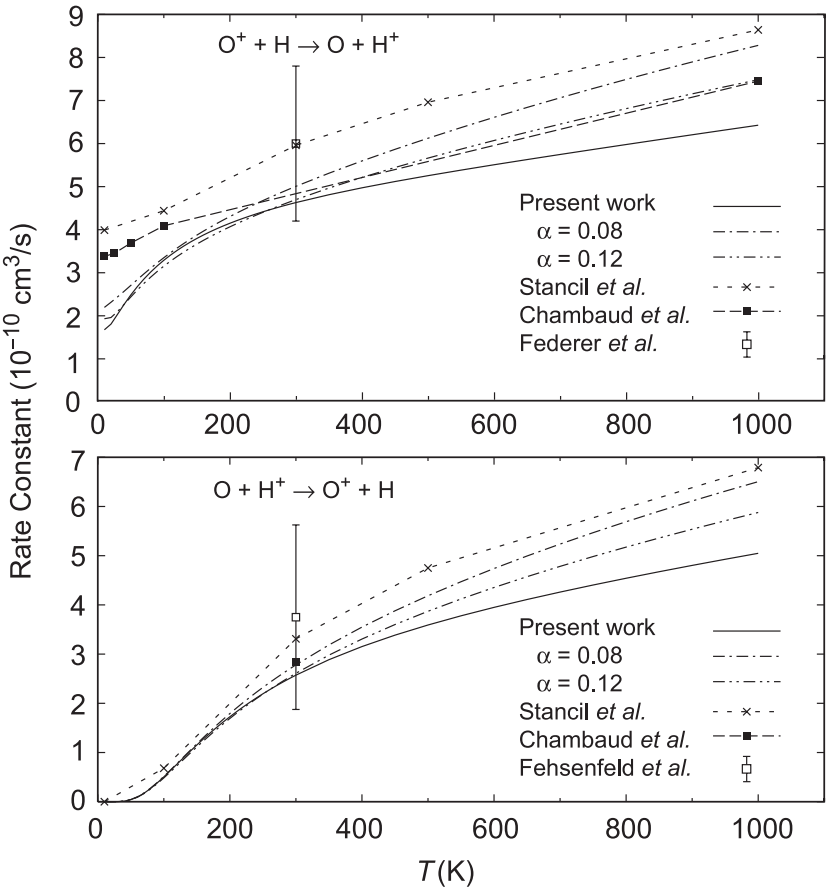

Figure 8. Comparison of the rate constants calculated in this work with other theoretical calculations and with experiment. The curves labelled $\alpha = 0.08$ and 0.12 were calculated with modified versions of $Q(R)$.

We have also shown the rate coefficients for our supplementary calculations in which the Massey parameter was modified. These rate coefficients, like the corresponding cross sections, have increased as the Massey parameter was decreased. This could indicate that the potentials used by Chambaud *et al* and by Stancil *et al* have a larger Massey parameter for the Demkov crossing near 11 a_0 discussed above.

The largest discrepancy between the results of various theories occurs at temperatures below 50 K and above 600 K. The theories happen to agree best near 300 K where the data are available. Additional experimental data would be useful for temperatures in the range from 600–1000 K. In addition, low-temperature (10–50 K) experiments would be useful, but only for $O^+ + H$. Because of the 158 cm^{-1} threshold for charge exchange from the $O(^3P_2) + H^+$ state, low-temperature collisions in that direction would not be particularly enlightening.

3.9. Comparison of diabatic Hamiltonians for $N_\alpha = 2$ and 3

The Hamiltonian matrix elements used in all the above calculations were the result of the 2×2 block diagonalization of the Hamiltonian matrix described in Spirko *et al* [5]. The

nomenclature used there was $N_\alpha = 2$. Additional calculations with $N_\alpha = 3$ and 4 were also reported. The latter calculation explicitly includes matrix elements involving the higher excited states of O and O^+, which correspond to closed channels for all the calculations performed here. Spirko *et al* [5] found that the matrix elements for the $N_\alpha = 3$ and 4 calculations were similar, but the $N_\alpha = 2$ results differed from them, particularly for small values of R. We investigated the effect of this difference by performing another set of scattering calculations using the $N_\alpha = 3$ matrix elements.

The actual matrix elements used for the new calculation were taken from the first 2×2 block of the $N_\alpha = 3$ matrix. This procedure corresponds to truncating the coupled channel expansion so it includes only open channels, but evaluating the matrix elements using diabatic electronic states determined with a larger expansion. One might argue that the diabatic states are then more accurately determined, but some are neglected. In contrast, the block diagonalization for $N_\alpha = 2$ attempts to modify the open-channel matrix elements in a way to account for the effect of closed channels. We do not know *a priori* which of these procedures is preferable. The most desirable method, of course, would be to include the entire $N_\alpha = 3$ matrix and to generalize the scattering calculations to include closed channels. That was beyond the scope of the present work.

We found that none of the state-to-state cross sections shown in figure 1 changed significantly. These results correspond to cross sections integrated over angle. For the P-dependent partial cross sections, which are summed according to equation (10), we found significant differences only for the $3/2 \rightarrow 1$ transition. Generally speaking, the fluctuations in the $3/2 \rightarrow 1$ partial cross sections were different for the two sets of potentials, but the sums were almost unchanged. It is likely that a calculation of differential (angle-dependent) cross sections would be sensitive to these differences.

4. Summary

We have used newly calculated diabatic potential curves to perform coupled channel scattering calculations for the collision $O + H^+ \leftrightarrow O^+ + H$. Cross sections and rate coefficients for a wide range of energies and temperatures were determined, and further calculations were performed to investigate possible mechanisms for the collision. By selectively modifying certain coupling terms, we gained insight into the relation between the cross sections and the potential curves. Several curve crossings were identified that provide plausible mechanisms for selected transitions.

One crossing that is important for the charge exchange process occurs near $R = 11\ a_0$, indicating that the potentials and couplings at that distance need to be accurately determined. Tests with the couplings modified for $R > 15\ a_0$ indicate that the inelastic transitions do not depend strongly on the potentials in this region.

Comparisons with previous theoretical calculations and with the limited experimental studies are not conclusive. Data are only available at 300 K and are highly averaged. The present theoretical calculations as well as those of Chambaud *et al* [3] and Stancil *et al* [4] all lie within the large error bars of the available data. Additional experimental data in the ranges $T = 10$–50 and 600–1000 K would be most useful to resolve the discrepancies between the theoretical calculations.

Acknowledgments

This work was supported by NSF Aeronomy grant ATM-9810645. JJZ was supported by the NSF REU site grant at Lehigh University.

References

[1] Fehsenfeld F C and Ferguson E E 1972 *J. Phys. Chem.* **56** 3066
[2] Federer W, Villinger H, Howorka F, Lindinger W, Tosi P, Bassi D and Ferguson E 1984 *Phys. Rev. Lett.* **52** 2084–6
[3] Chambaud G, Launay J M, Levy B, Millie P, Roueff E and Tran Minh F 1980 *J. Phys. B: At. Mol. Phys.* **13** 4205–16
[4] Stancil P C, Schultz D R, Kimura M, Gu J P, Hirsch G and Buenker R J 1999 *Astron. Astrophys. Suppl. Ser.* **140** 225–34
[5] Spirko J A, Mallis J T and Hickman A P 2000 *J. Phys. B: At. Mol. Opt. Phys.* **33** 2395–407
[6] Saxon R P and Liu B 1986 *J. Chem. Phys.* **85** 2099–104
[7] Cohen J S and Schneider B I 1974 *J. Chem. Phys.* **61** 3230–9
[8] Hickman A P, Medikeri-Naphade M, Chapin C D and Huestis D L 1997 *Phys. Rev.* A **56** 4633–43
[9] Curtiss C F and Adler F T 1952 *J. Chem. Phys.* **20** 249–56
[10] Walker R B and Light J C 1975 *Chem. Phys.* **7** 84–93
[11] Launay J M 1977 *J. Phys. B: At. Mol. Phys.* **10** 3665–72
[12] Johnson B R 1973 *J. Comput. Phys.* **13** 445–9
[13] Olson R E 1980 *Comment. At. Mol. Phys.* **9** 231–8
[14] Massey H S W 1949 *Rep. Prog. Phys.* **12** 248
[15] Spirko J A and Hickman A P 1999 *Bull. Am. Phys. Soc.* **44** 1102
[16] Stancil P C 2000 Corrections to cross sections, private communication